

Homogeneous Free-Standing Nanostructures from Bulk Diamond over Millimeter Scales for Quantum Technologies

Andrea Corazza, Silvia Ruffieux, Yuchun Zhu, Claudio A. Jaramillo Concha, Yannik Fontana, Christophe Galland, Richard J. Warburton, and Patrick Maletinsky*



Cite This: *Nano Lett.* 2025, 25, 14526–14533



Read Online

ACCESS |

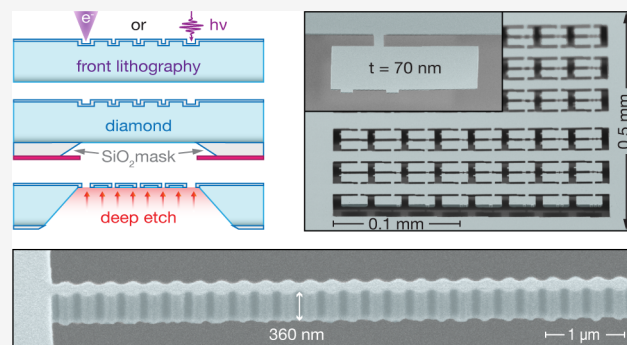
Metrics & More

Article Recommendations

Supporting Information

ABSTRACT: Quantum devices based on optically addressable spin qubits in diamond are promising platforms for quantum technologies such as quantum sensing and communication. Nano- and microstructuring of the diamond crystal is essential to enhance device performance, yet fabrication remains challenging and often involves trade-offs in surface quality, aspect ratio, device size, and uniformity. We tackle this hurdle with an approach producing millimeter-scale, thin (down to 70 nm), and highly parallel (< 0.35 nm/ μm) membranes from single-crystal diamond. The membranes remain contamination free and possess atomically smooth surfaces ($R_q < 200$ pm) as required by state-of-the-art quantum applications. We demonstrate the benefits and versatility of our method by fabricating large fields of free-standing and homogeneous photonic nano- and microstructures. Leveraging a refined photolithography-based strategy, our method offers enhanced scalability and produces robust structures suitable for direct use, while remaining compatible with heterogeneous integration through pick-and-place transfer techniques.

KEYWORDS: *Diamond nanostructures, Diamond photonics, Quantum communication, Quantum sensing, Photonic crystal cavities, Optical lithography*

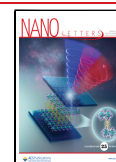


Diamond's unparalleled properties make it an enticing choice for a plethora of applications, including low-loss microelectro-mechanical systems,^{1–3} high-power electronics and optics,^{4–7} as well as quantum photonics, phononics, and sensing.^{8–10} Notably, diamond can incorporate a variety of optically active point defects (color centers) that also exhibit coherent ground-state spins.^{11,12} The intrinsic spin-photon interface provided by color centers in single-crystal diamond has enabled multiple breakthroughs pertaining to quantum registers and networks.^{13–17} Additionally, their spin can serve as powerful sensors either as ensembles^{18–20} or at the single center level.^{21–23} At the core of most of these achievements is the ability to process diamond at the micro- and nanoscale. Novel fabrication methods enabled advanced diamond quantum devices such as micrometer-thin membranes for heterogeneous photonics,^{24–28} all diamond scanning probe sensors,^{29–32} mechanical resonators,^{1,33–37} and monolithic nanophotonic waveguides and photonic crystal (PhC) cavities.^{38–41} However, in several aspects, fabrication hurdles continue to limit the performance and scalability of these devices. Specifically, obtaining high-quality, extended, and homogeneous arrays of devices with arbitrary geometries while maintaining a high yield and integration potential remains a stumbling block. Additionally, for color center-based devices,

magnetic and charge fluctuators located on processed surfaces lead to a degradation of the spin and optical coherence of the color centers, emphasizing the need for well-terminated, atomically smooth diamond surfaces.^{42,43}

The fabrication of released, free-standing devices is a key aspect of this challenge, and several methods have emerged to address it.^{44–46} Angled-etching^{47–49} and quasi-isotropic etching^{50–52} rely on under-etching of structures fabricated on bulk diamond surfaces and work best for low-dimensional, thin structures or devices supported by a pedestal. The downsides of either are the tendency to produce suboptimal surface quality (increased roughness) and the inability to obtain arbitrarily flat back surfaces, compromising the device performance.⁴¹ A different strategy to produce diamond membranes with thicknesses matching the device requirement proceeds via a “smart-cut” process combined with diamond epitaxy.^{53,54} This method yields thin membranes, typically

Received: June 11, 2025
Revised: August 21, 2025
Accepted: August 26, 2025
Published: September 26, 2025



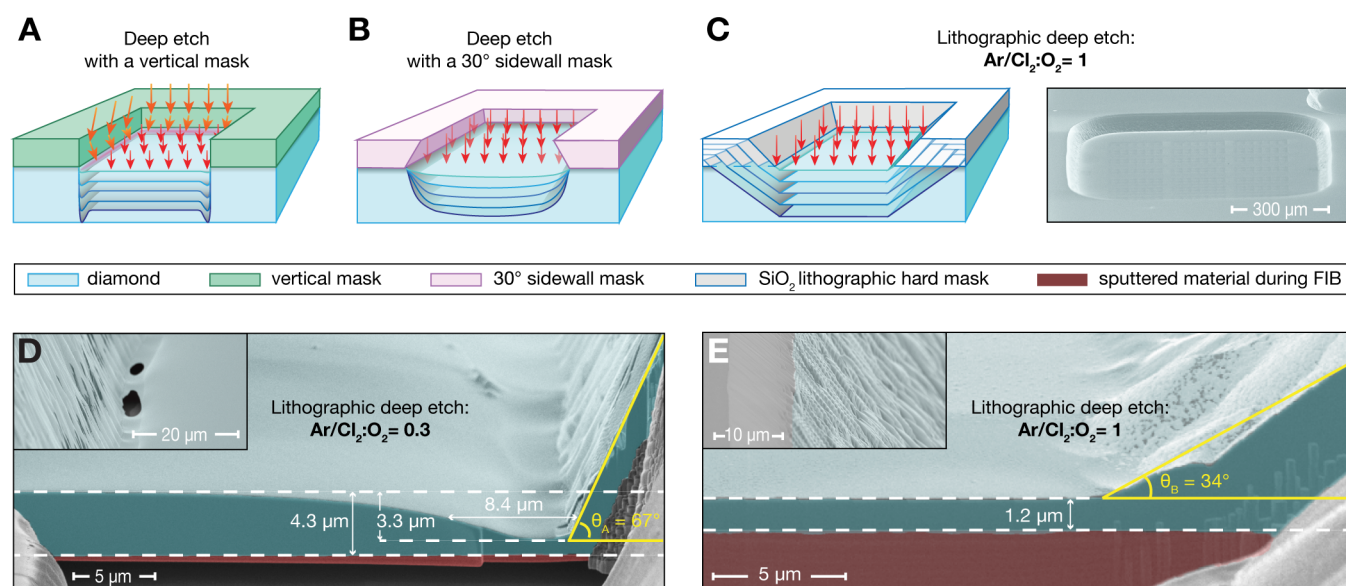


Figure 1. Diamond membrane processing. (A) A vertical hard mask (green) and vertical diamond (blue) sidewall confine the etching plasma (orange arrows) at the edges of the etching pit, leading to the formation of trenches. (B) A mask with $\sim 30^\circ$ sidewalls (pink) decreases the etching plasma density (faded red arrows) at the edges of the etching pit, mitigating the formation of trenches but introducing thickness gradients in the membrane. (C) Left: Evolution of the etching pit profile using an Ar/Cl₂:O₂ ratio of 1. The angled sidewall of the pit, created by etching the SiO₂ mask during the Ar/Cl₂ steps, mitigates plasma confinement and prevents trench formation. Right: SEM micrograph (taken at 70° viewing angle) of a $\sim 45 \mu\text{m}$ deep etching pit. The resulting diamond membrane has an area of $\sim 760 \times 760 \mu\text{m}^2$ and a thickness of $1.2 \mu\text{m}$. (D) SEM micrograph (same imaging angle) of the membrane thickness profile near the etching pit sidewall for an Ar/Cl₂:O₂ ratio of 0.3. The trench is $3.3 \mu\text{m}$ deep and $8.4 \mu\text{m}$ wide at half-depth. Inset: Perforation of the membrane due to trenching, compromising its mechanical stability. (E) Same as (D), but for an Ar/Cl₂:O₂ ratio of 1. No trenches are visible. Inset: Profile of the etching pit sidewall and of the SiO₂ mask during etching. Terraces form due to different selectivity of the Ar/Cl₂ and O₂ plasma.

ranging from tens to a few hundred nanometers,^{55,56} with higher surface quality compared to the underetching methods. However, the smart-cut approach is complex and resource intensive, and the membranes are completely disconnected from the bulk diamond and therefore need to be rebonded to a carrier.⁵⁷

A more straightforward procedure for fabricating free-standing devices involves deep etching of a bulk diamond over an area defined by macroscopic shadow masks. By this approach, membranes can be created on millimeter scales, with low-roughness surfaces and a diamond quality limited only by the starting material.^{30,58} Yet, obtaining submicrometer thicknesses and low gradients across the entire etched membrane is highly challenging because of geometry-induced plasma enhancement effects^{59,60} that result in micrometer-deep trench build-ups along the membrane's perimeter (Figure 1A). Consequently, the minimum achievable thickness of the free-standing structures is limited. Reduction of the plasma flux near the sidewalls can be achieved using a shadow mask with $\sim 30^\circ$ sidewalls (wider opening facing the diamond, Figure 1B); however, this method still produces significant thickness gradients that are dependent on the mask geometry.^{34,60} Additionally, achieving accurate mask alignment and reliable mask fixation during the deep etch process remains challenging.⁵⁸

In addition to the ability to create thin structures, precise and efficient micro- and nanoscale patterning of diamond surfaces is essential for fabricating diamond-based quantum devices. Diamond's hardness and chemical inertness demand mask materials with high chemical selectivity to transfer accurately the designed patterns.⁴⁴ Techniques such as electron beam lithography (EBL)^{47,51} and focused ion beam

(FIB) milling^{61,62} have been successfully used to fabricate photonic crystal nanocavities and waveguides. However, while achieving high accuracy and resolution, these methods are resource intensive and inefficient for large-scale patterning of micrometer-sized structures, such as scanning probe sensors³⁰ and platelets for heterogeneous photonic devices.²⁴ Additionally, ion beam irradiation risks damaging the diamond surface and embedded color centers. Optical lithography is a fast and scalable alternative, and it has already been used to pattern diamond structures.^{31,63,64} However, further development is needed to reproducibly reach the submicrometer resolution required to break out free-standing quantum devices by pick-and-place techniques.

In this work, we present first an improved fabrication strategy, the "lithographic deep etch" (LDE), to produce large-scale free-standing thin membranes. The LDE 1) eliminates problems with trench formation and thickness inhomogeneities, 2) enables high-accuracy positioning of the area to be deep-etched, and 3) allows us to define multiple etching windows of arbitrary shapes on one and the same diamond. To demonstrate the potential of this method for quantum photonics, we pattern the front surface of bulk diamonds with micro- and nanostructures (diamond platelets for heterogeneous integration and PhC cavities, respectively) that are subsequently released from the back by a deep etch. The free-standing structures we obtain have a submicrometer thickness (down to 70 nm) with a residual gradient limited only by the initial wedge of the diamond plate. They are compatible with pick-and-place transfer techniques while remaining supported by a frame robust enough for manual manipulation. In a second part, we present a fast, simple, and scalable approach using optical lithography combined with an

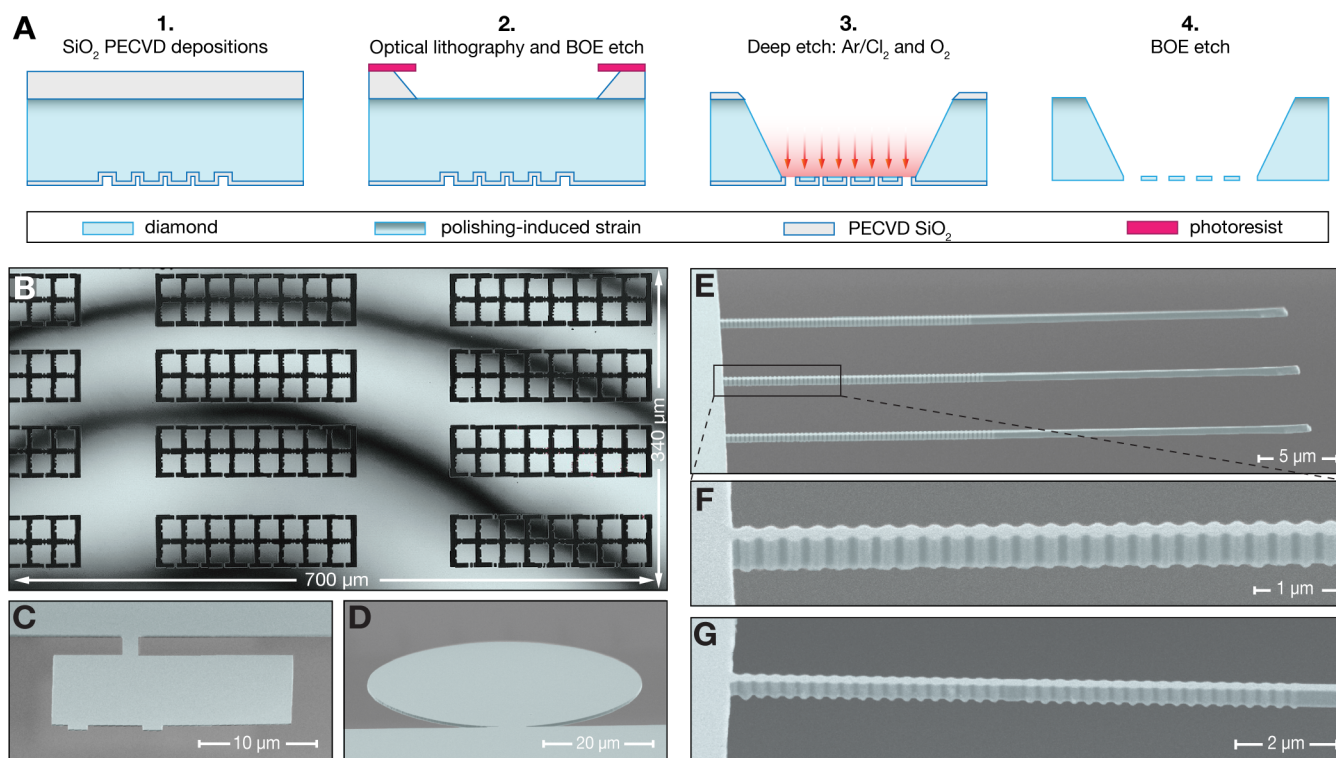


Figure 2. (A) Fabrication flow for the LDE process. (1) After the front pattern definition, the front surface is protected with a thin layer of SiO₂ and the thick deep etch mask (10–22 μm of SiO₂, light gray) is deposited on the backside. (2) Definition of the etching windows via optical lithography and a BOE etch to transfer the pattern to the hard mask. (3) Photoresist removal and ICP-RIE deep etch using Ar/Cl₂ and O₂ to release the nanostructures. (4) BOE etch to remove the hard mask. (B) Laser scanning confocal microscope ($\lambda = 404$ nm) image of a 700 × 340 μm² region of the deep-etched side of a 2 × 1 mm² free-standing membrane patterned with platelets. The membrane has a wedge less than 0.6 nm/μm along the highest thickness gradient direction. The thickness difference between fringes is 84 nm. (C) SEM micrograph of a single 70 nm thick free-standing platelet. (D) SEM micrograph of a 50 μm diameter disk with a thickness of 500 nm. (E) SEM micrograph of 360 nm thick free-standing tapered waveguides with distributed Bragg reflectors (DBR) and anchor point to the holding structure of one of the waveguides shown in (E). (F) Zoom in on the DBR and anchor point to the holding structure of one of the waveguides shown in (E). (G) SEM micrograph of a 350 nm thick free-standing tapered PhC cavity. All SEM images were obtained at a 70° viewing angle. The front pattern definition in (B) was done by optical lithography, while EBL was used to pattern the structures in (C)–(G).

active feedback focusing system to define the front pattern of microstructures into diamond. To demonstrate its capability, we fabricate arrays of diamond platelets for heterogeneous integration and cantilevers for scanning-probe sensors, achieving submicrometer resolution.

The LDE process for creating large-scale free-standing membranes from a bulk diamond (~50 μm) relies on creating a thick SiO₂ lithographic mask with outward-slanted sidewalls that retract as the deep etch progresses (Figure 1C). Our inductively coupled plasma reactive ion etching (ICP-RIE) recipe relies on alternating Ar/Cl₂ and O₂ plasmas.²⁹ The former mostly leads to a smoothing of the diamond surface, while the latter produces a fast, anisotropic etch of the diamond. Crucially, Ar/Cl₂ also etches aggressively SiO₂. Thus, tuning the etching time ratio of the plasmas allows for controlled lateral retraction of the SiO₂ mask. As a result, the angle of the etching pit's sidewalls can be tuned, preventing plasma confinement and the formation of trenches. The mechanism that avoids the trench formation during the LDE is shown in Figure 1C, together with a typical 45 μm deep etching pit resulting from our process, here with an area of 760 × 760 μm². The diamond membrane is 1.2 μm thick. To characterize how the membrane thickness profile close to the diamond sidewall evolves as a function of the Ar/Cl₂:O₂ content, we mill an inspection slot in the proximity of the etching pit sidewall via a focused ion beam (FIB) to access the

trench profiles. In Figure 1D, where a diamond pit etched with an Ar/Cl₂:O₂ ratio of 0.3 is shown, a trench with a depth of 3.3 μm and a width of 8.4 μm at half its depth is measured. The angle of the diamond etching pit sidewall from the sample plane is 67°, showing that the plasma confinement, although mitigated, is still present and induces higher etching rates along the membrane perimeter and eventually leads to perforation (see inset of Figure 1D). Increasing the Ar/Cl₂:O₂ ratio to one decreases the diamond etching pit sidewall angle close to the membrane to 34° (Figure 1E), while the sidewall has an average angle of ~45° (inset Figure 1E). At this sidewall angle, the reflected ions at grazing angles no longer reach the diamond membrane but hit the sidewall such that no trench build-up is observed. In the inset of Figure 1E the diamond terraces, created by alternating the two plasmas, as well as the SiO₂ lithographic mask are visible.

To integrate patterns needed for quantum devices into the diamond membrane, two approaches can be employed. In the first approach, the design (“front lithography”) is patterned prior to membrane release, while in the second, patterning is performed after the creation of a thin diamond membrane. For the fabrication of submicrometer free-standing diamond nanostructures, we adopt the first approach to avoid potential damage to the fragile membrane during lithography. The fabrication process for the LDE following the front pattern definition is illustrated in Figure 2A. First, we use plasma-

enhanced chemical vapor deposition (PECVD) to deposit a layer of SiO₂ (50–100 nm) to protect the front design, flip the sample, and deposit a thick (10–22 μm) layer of SiO₂ as hard mask for the deep etch. Second, optical lithography is performed to define the etching windows (see Supporting Information (SI)), and the design is transferred to the hard mask via a buffered oxide etchant (BOE) 10:1 etch. The isotropic wet etch guarantees outward-slanted sidewalls with angles much lower than ~45° near the diamond surface. This enables the hard mask to retract in the third step, in which the diamond is etched with alternating Ar/Cl₂ and O₂ plasmas in an ICP-RIE reactor. Fourth, once the desired membrane thickness is achieved, the mask is removed with a BOE (10:1) etch.

We characterize the thickness gradient of the free-standing membranes using a laser scanning confocal microscope (Keyence VK-X1100, λ = 404 nm). The measured wedge is consistent with that observed for the diamond plate before the LDE (see SI Figure S3) and is solely determined by the intrinsic thickness gradient introduced during laser slicing and polishing. Thus, unlike deep etching approaches based on bulk masks,^{58,60,65,66} the LDE process does not introduce any additional thickness inhomogeneities. We quantify the wedge within a 700 × 340 μm² region of a free-standing membrane patterned with platelets in Figure 2B knowing that the thickness difference between two destructive interference fringes is λ/2n_d = 84 nm, where n_d is the refractive index of diamond. The entire membrane has a wedge below 0.6 nm/μm along the direction of the highest thickness gradient. By characterizing the thickness gradient of the diamond plate before patterning devices, owing to the lithographic nature of the LDE, one can exploit the intrinsic wedge for tuning the thickness of the quantum devices. Over a 1 mm² region, we measured wedges down to 0.35 nm/μm along the highest thickness gradient direction (see SI Figure S3), which projected on the typical size of our Fabry–Pérot microcavity platelets,^{24,27} 20 × 20 μm², leads to a maximal thickness difference of 7 nm.

The absence of a trench and the flexibility of the LDE process enable the fabrication of free-standing diamond structures with arbitrary thicknesses and size. As visible in Figure 2C, extended free-standing areas as thin as 70 nm (see SI Figure S4) can be realized, demonstrating this method as a highly competitive alternative to smart-cut techniques. Moreover, the LDE process enables the creation of flat structures connected to a supporting frame and with arbitrary in-plane aspect ratios, exemplified in Figure 2D—which are beyond the reach of conventional angled-etching or quasi-isotropic etching methods. To demonstrate the potential of this approach, we fabricate some of the most demanding structures required for diamond-based quantum technologies, where stringent control over morphology and roughness of the back surface is critical. Specifically, we realize two distinct types of free-standing nanostructures, each with a thickness of 350–360 nm: tapered waveguides with distributed Bragg reflectors (DBRs) and tapered photonic crystal (PhC) cavities. Both designs are optimized for a target wavelength of 1042 nm, corresponding to the nitrogen-vacancy (NV) center's singlet transition, with an ideal thickness of 355 nm. The full length of three tapered waveguides with DBRs is presented in Figure 2E, while a magnified view highlighting the DBR structure and the anchor points to the holding framework is shown in Figure 2F. Additionally, Figure 2G displays an SEM image of the two

DBRs forming a PhC cavity, further illustrating the precision and viability of our fabrication process.

We characterize the surface morphology of the deep-etched side of the diamond nanostructures by using atomic force microscopy (AFM). To facilitate this, free-standing diamond platelets, approximately 900 nm thick, were released and bonded to a silicon chip via van der Waals forces, with the deep-etched surface facing upward (see SI Sec. IV). The morphology and roughness of this surface are compared to those of the front surface, which only underwent a 4 μm stress-relief etch to remove crystal damage introduced by the polishing.³⁰ It is important to note that the plasma chemistry used for the deep etch closely mimics that employed to achieve state-of-the-art stress-relieved diamond surfaces, utilizing alternating Ar/Cl₂ and O₂ plasmas (see SI Sec. I). Figure 3A

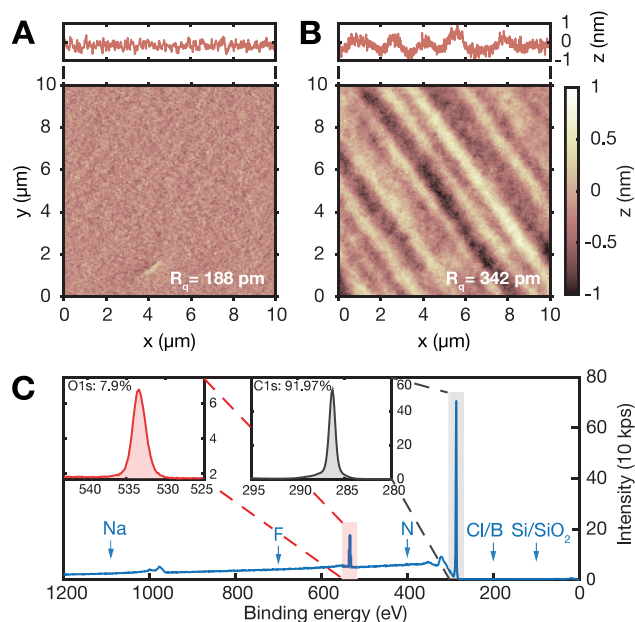


Figure 3. (A) AFM scan of the stress-relieved front diamond surface over an area of 10 × 10 μm². The measured RMS roughness (R_q) is 188 pm. No increase of R_q is observed with the size of the AFM scan (see Supporting Information (SI) Figure S1D). (B) AFM of the deep-etched diamond surface of a ~900 nm thin platelet over an area of 10 × 10 μm². The R_q is 342 pm, while for an area of 1 × 1 μm² is 198 pm. The higher surface roughness is due to different polishing performed on the two surfaces (see SI Figure S1E). (c) XPS survey measurement of the deep-etched surface of a diamond membrane after the LDE. Inset: High-resolution scans of the C 1s and O 1s peaks. The diamond has no contamination and is oxygen terminated after the triacid cleaning with approximately a monolayer of coverage.

presents an AFM scan of the front surface after stress relief, revealing a remarkably low surface roughness (R_q) of 188 pm, even over an area of 10 × 10 μm². Notably, there is no significant increase in R_q when comparing a 1 × 1 μm² scan (187 pm) to a 10 × 10 μm² scan (see SI Figure S1D). This long-range flatness over tens of square micrometers is attributed to the combination of the stress-relief etching process and an improved diamond polishing technique developed by Almax easyLab (Belgium), which already yields surfaces with a roughness of approximately 200 pm after polishing (see SI Figure S1B). The exceptional surface quality and flatness of the released diamond micro- and nanostructures hold promise for photonics and quantum device applications,

as polishing-induced surface waviness is a major limiting factor in achieving high Q -factors in diamond-based Fabry–Pérot microcavities.⁶⁷ Figure 3B shows a $10 \times 10 \mu\text{m}^2$ AFM scan of the deep-etched surface, revealing a surface roughness of 342 pm. While this initially suggests an increase in roughness due to the deep etch, it is crucial to consider that the back surface, before deep etching, had undergone a different polishing process performed by Almax easyLab, resulting in a significantly higher initial roughness of 976 pm over a $10 \times 10 \mu\text{m}^2$ area (see SI Figure S1A). To allow for a fair comparison, we applied our standard stress-relief etch to a diamond sample that underwent the same initial polishing as the deep-etched surface. The resulting R_q value of 587 pm indicates that the deep etch effectively smoothens the waviness induced by polishing, even more so than the stress-relief etch (see SI Figure S1C). Finally, it is worth noting that polishing-induced waviness becomes relevant only for surface areas larger than $1 \times 1 \mu\text{m}^2$, as at that scale, R_q remains below 200 pm for all considered cases.

The deep-etched back surface was further analyzed by using X-ray photoelectron spectroscopy (XPS) with a beam size of $250 \mu\text{m}^2$ and compared to the front surface. The corresponding XPS survey shown in Figure 3C is identical to that of a stress-relieved surface, exhibiting no detectable contamination. The high-resolution scan of the O 1s peak confirms oxygen termination, with a coverage of approximately one monolayer, consistent with the expected outcome of the triacid cleaning process (refluxing mixture of concentrated perchloric, nitric, and sulfuric acids).⁴² Additionally, the high-resolution scan of the C 1s peak shows no detectable low-energy shoulder, indicating a minimal presence of sp^2 carbon bonds. These bonds are known to lead to deep traps that, in turn, induce surface magnetic and charge noise, which can degrade the spin and optical coherence of shallow optically active spin defects in diamond.⁴² The absence of contaminants and the low content of sp^2 carbon-related deep traps confirm the state-of-the-art surface quality achieved by the LDE process.

To assess the relevance of our fabrication approach for quantum photonic devices hosting spin defects, we quantified the charge-noise environment in the fabricated structures, the dominant optical decoherence source for emitters near etched surfaces. This surface noise has motivated alternative approaches that integrate heterogeneous photonic structures with bulk diamond.^{68–71} Using NV centers as sensitive electrometers, we measure the NV centers' extrinsic optical linewidth in submicrometer-thick platelets and infer an rms electric-field noise of $\sim 7.4 \text{ kV m}^{-1}$ (see SI Sec. V), comparable to state-of-the-art results.^{72–74} For centrosymmetric defects such as the tin-vacancy center, this noise level would broaden the lifetime-limited linewidth by at most 1% (see SI Sec. V), having therefore a negligible impact on their optical coherence.

Next, we focus on the optical lithography process we developed to efficiently define the front pattern of the diamond microstructures. This method relies on focusing the laser of a direct laser writing (DLW) system onto the photoresist, thereby writing the desired pattern, and transferring the pattern to a SiO_2 hard mask that ensures chemical resistance to O_2 plasma etching, thereby maintaining high pattern fidelity throughout the process. The fabrication process is illustrated in Figure 4A. We begin with the PECVD deposition of a 300 nm SiO_2 etch mask and a 60 nm Si layer to facilitate laser focusing. Due to the transparency of both the diamond plate and the

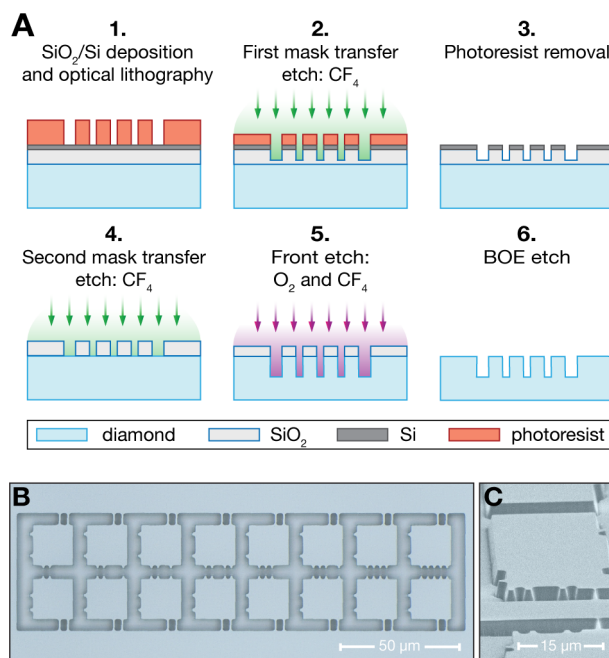


Figure 4. (A) Fabrication flow for the DLW optical lithography and front etching of diamond microstructures. (1) PECVD deposition of the etch mask (300 nm of SiO_2) and of a 60 nm Si layer for focusing the writing laser. After spin coating the photoresist, DLW optical lithography is performed. (2) Pattern transfer to the SiO_2/Si layers through a CF_4 ICP-RIE etch. The etch is calibrated to stop a few tens of nm before etching through the SiO_2 layer to avoid contamination and micromasking of the diamond surface. (3) Photoresist removal through acetone and piranha cleaning. (4) The remaining few tens of nm of SiO_2 and the Si layer are removed with CF_4 . (5) Pattern transfer to the diamond front surface via O_2 and CF_4 etches. (6) SiO_2 removal with a BOE etch. (B) Micrograph after pattern definition of $20 \times 20 \mu\text{m}^2$ platelets with $1 \mu\text{m}$ wide bridges via optical lithography. (C) SEM micrograph after pattern definition of $20 \times 40 \mu\text{m}^2$ cantilevers with 200 nm wide bridges via optical lithography.

SiO_2 layer, the Si layer is essential to provide the optical contrast needed to focus reliably the feedback laser in the DLW system on the top surface. The DLW optical lithography is performed using a positive photoresist (see SI Sec. IIA), and the pattern is transferred to the SiO_2/Si layers via a CF_4 plasma ICP-RIE etch. To prevent contamination and micromasking of the diamond surface, the etch is calibrated so that it stops a few tens of nanometers before reaching the diamond, allowing for photoresist removal. The remaining SiO_2 and Si focusing layers are then fully removed by a final CF_4 etch, completing the definition of the etch mask. The pattern is subsequently transferred into the diamond using an O_2 and CF_4 plasma ICP-RIE etch, after which the mask is removed via a BOE etch. AFM and XPS measurements confirm that this process does not introduce any contamination or increase the surface roughness.

To evaluate our fabrication process, we pattern a $4 \times 4 \text{ mm}^2$ area of the diamond surface with $20 \times 20 \mu\text{m}^2$ platelets (see SI Figure S2), each connected to the holding structure by $1 \mu\text{m}$ -wide bridges, compatible with pick-and-place transfer into a Fabry–Pérot optical microcavity.²⁷ A portion of the patterned area is shown in Figure 4B. Additionally, to assess the minimum feature size achievable using positive-tone lithography, we fabricate cantilevers for scanning NV magnetometry,²² achieving bridge widths as small as 200 nm (Figure

4C). By leveraging optical lithography with a positive-tone resist and a robust hard-mask transfer technique, we overcome the major limitations of conventional EBL-based approaches, enabling submicrometer resolution over millimeter-scale areas with significantly reduced processing time.

In conclusion, we have demonstrated the fabrication of large-scale, homogeneous, submicrometer thick, free-standing nano- and microstructures from single-crystal bulk diamond, tailored for integrated quantum technologies. A key challenge in deep-etching processes, trench build-up caused by plasma confinement near the mask and diamond etching pit sidewalls, was systematically investigated and mitigated through a lithographic SiO₂ mask. As a result, we achieved lithographically defined millimeter-scale membranes with thickness gradients as low as 0.35 nm/ μ m, limited only by the initial wedge of the diamond plate after polishing. This enables the deterministic release of highly uniform nano- and microstructures with thicknesses down to 70 nm. Comprehensive characterization confirms the exceptional quality of the fabricated structures, with atomically smooth, contamination-free surfaces ($R_q < 200$ pm) and a low level of charge noise (~ 7.4 kV, rms), ideal for hosting coherent spin defects. Additionally, the resulting nano- and microstructures are compatible with pick-and-place transfer techniques, facilitating integration with heterogeneous material platforms.

To further advance diamond microfabrication, we developed a refined patterning approach based on DLW optical lithography, significantly reducing writing times, simplifying fabrication equipment, and enabling scalable, high-resolution structuring over large areas, making it a promising candidate for large-scale quantum device fabrication. These advancements mark a significant step toward scalable and high-performance diamond-based quantum technologies.

■ ASSOCIATED CONTENT

SI Supporting Information

The Supporting Information is available free of charge at <https://pubs.acs.org/doi/10.1021/acs.nanolett.5c03083>.

Detailed description of the fabrication process: sample preparation and stress relief etch with AFM characterization, front pattern definition, lithographic deep etch with thickness gradient characterization, and thinnest platelet measurement. Description of the platelet breakout process for AFM characterization. Characterization and discussion of optical properties of color centers in submicrometer platelets. (PDF)

■ AUTHOR INFORMATION

Corresponding Author

Patrick Maletinsky – Department of Physics, University of Basel, CH-4056 Basel, Switzerland; orcid.org/0000-0003-1699-388X; Email: patrick.maletinsky@unibas.ch

Authors

Andrea Corazza – Department of Physics, University of Basel, CH-4056 Basel, Switzerland; orcid.org/0000-0003-2750-3049

Silvia Ruffieux – Department of Physics, University of Basel, CH-4056 Basel, Switzerland; orcid.org/0000-0002-8904-8195

Yuchun Zhu – Institute of Physics and Center for Quantum Science and Engineering, Ecole Polytechnique Fédérale de Lausanne (EPFL), 1015 Lausanne, Switzerland

Claudio A. Jaramillo Concha – Institute of Physics and Center for Quantum Science and Engineering, Ecole Polytechnique Fédérale de Lausanne (EPFL), 1015 Lausanne, Switzerland

Yannik Fontana – Department of Physics, University of Basel, CH-4056 Basel, Switzerland

Christophe Galland – Institute of Physics and Center for Quantum Science and Engineering, Ecole Polytechnique Fédérale de Lausanne (EPFL), 1015 Lausanne, Switzerland; orcid.org/0000-0001-5627-0796

Richard J. Warburton – Department of Physics, University of Basel, CH-4056 Basel, Switzerland; orcid.org/0000-0002-3095-3596

Complete contact information is available at:

<https://pubs.acs.org/10.1021/acs.nanolett.5c03083>

Notes

The authors declare no competing financial interest.

■ ACKNOWLEDGMENTS

We thank Gerard Gadea Diez for fruitful discussions regarding the Si and the thick SiO₂ PECVD depositions, Marcus Wyss for the FIB milling, Kexin Wu for his contribution to the lithographic design, Marina Obramenko for her contribution to the linewidth measurements, and the Swiss Nanoscience Institute for providing and maintaining much of the fabrication infrastructure. We acknowledge financial support by the ERC consolidator grant project QS2DM and by the SERI Swiss quantum transitional call project “QuantumLeap”. A.C. acknowledges financial support from the Quantum Science and Technologies at the European Campus (QUSTEC) project of the European Union’s Horizon 2020 research and innovation program under the Marie Skłodowska-Curie Grant Agreement No. 847471. Y.Z., C.A.J.C., and C.G. acknowledge funding from the Swiss National Science Foundation, Grants No. 198898 and No. 204036.

■ REFERENCES

- (1) Tao, Y.; Boss, J. M.; Moores, B. A.; Degen, C. L. Single-crystal diamond nanomechanical resonators with quality factors exceeding one million. *Nat. Commun.* **2014**, *5*, 3638.
- (2) Wu, H.; Sang, L.; Li, Y.; Teraji, T.; Li, T.; Imura, M.; You, J.; Koide, Y.; Toda, M.; Liao, M. Reducing intrinsic energy dissipation in diamond-on-diamond mechanical resonators toward one million quality factor. *Phys. Rev. Mater.* **2018**, *2*, 090601.
- (3) Zhang, Z.; Gu, K.; Toda, M.; Liao, M. A perspective on diamond mems magnetic sensors. *Appl. Phys. Lett.* **2025**, *126*, 100501.
- (4) Zhu, T.-F.; Fu, J.; Wang, W.; Wen, F.; Zhang, J.; Bu, R.; Ma, M.; Wang, H.-X. Fabrication of diamond microlenses by chemical reflow method. *Opt. Express* **2017**, *25*, 1185.
- (5) Donato, N.; Rouger, N.; Pernot, J.; Longobardi, G.; Udrea, F. Diamond power devices: state of the art, modelling, figures of merit and future perspective. *J. Phys. D: Appl. Phys.* **2020**, *53*, 093001.
- (6) Sasama, Y.; Kageura, T.; Imura, M.; Watanabe, K.; Taniguchi, T.; Uchihashi, T.; Takahide, Y. High-mobility p-channel wide-bandgap transistors based on hydrogen-terminated diamond/hexagonal boron nitride heterostructures. *Nat. Electron.* **2022**, *5*, 37.
- (7) Hasan, M. M.; Wang, C.; Pala, N.; Shur, M. Diamond for high-power, high-frequency, and terahertz plasma wave electronics. *Nanomaterials* **2024**, *14*, 460.

- (8) Schröder, T.; Mouradian, S. L.; Zheng, J.; Trusheim, M. E.; Walsh, M.; Chen, E. H.; Li, L.; Bayn, I.; Englund, D. Quantum nanophotonics in diamond. *J. Opt. Soc. Am. B* **2016**, *33*, B65.
- (9) Shandilya, P. K.; Flagan, S.; Carvalho, N. C.; Zohari, E.; Kavatamane, V. K.; Losby, J. E.; Barclay, P. E. Diamond Integrated Quantum Nanophotonics: Spins, Photons and Phonons. *J. Light Technol.* **2022**, *40*, 7538.
- (10) Rovny, J.; Gopalakrishnan, S.; Jayich, A. C. B.; Maletinsky, P.; Demler, E.; de Leon, N. P. Nanoscale diamond quantum sensors for many-body physics. *Nat. Rev. Phys.* **2024**, *6*, 753.
- (11) Doherty, M. W.; Manson, N. B.; Delaney, P.; Jelezko, F.; Wrachtrup, J.; Hollenberg, L. C. The nitrogen-vacancy colour centre in diamond. *Phys. Rep.* **2013**, *528*, 1.
- (12) Thiering, G.; Gali, A. Color centers in diamond for quantum applications. In *Diamond for Quantum Applications Part 1, Semiconductors and Semimetals*, Vol. 103; Nebel, C. E., Aharonovich, I., Mizuochi, N.; Hatano, M., Eds.; Elsevier, 2020; pp 1–36.
- (13) Bernien, H.; Hensen, B.; Pfaff, W.; Koolstra, G.; Blok, M. S.; Robledo, L.; Taminiau, T. H.; Markham, M.; Twitchen, D. J.; Childress, L.; Hanson, R. Heralded entanglement between solid-state qubits separated by three metres. *Nature* **2013**, *497*, 86.
- (14) Bradley, C. E.; Randall, J.; Abobeih, M. H.; Berrevoets, R. C.; Degen, M. J.; Bakker, M. A.; Markham, M.; Twitchen, D. J.; Taminiau, T. H. A Ten-Qubit Solid-State Spin Register with Quantum Memory up to One Minute. *Phys. Rev. X* **2019**, *9*, 31045.
- (15) Bhaskar, M. K.; Riedinger, R.; Machielse, B.; Levonian, D. S.; Nguyen, C. T.; Knall, E. N.; Park, H.; Englund, D.; Lončar, M.; Sukachev, D. D.; Lukin, M. D. Experimental demonstration of memory-enhanced quantum communication. *Nature* **2020**, *580*, 60.
- (16) Pompili, M.; Hermans, S. L. N.; Baier, S.; Beukers, H. K. C.; Humphreys, P. C.; Schouten, R. N.; Vermeulen, R. F. L.; Tiggelman, M. J.; dos Santos Martins, L.; Dirkse, B.; Wehner, S.; Hanson, R. Realization of a Multi-Node Quantum Network of Remote Solid-State Qubits. *Science* **2021**, *372*, 259.
- (17) Stas, P. J.; Huan, Y. Q.; Machielse, B.; Knall, E. N.; Suleymanzade, A.; Pingault, B.; Sutula, M.; Ding, S. W.; Knaut, C. M.; Assumpcao, D. R.; Wei, Y. C.; Bhaskar, M. K.; Riedinger, R.; Sukachev, D. D.; Park, H.; Lončar, M.; Levonian, D. S.; Lukin, M. D. Robust multi-qubit quantum network node with integrated error detection. *Science* **2022**, *378*, 557.
- (18) Wolf, T.; Neumann, P.; Nakamura, K.; Sumiya, H.; Ohshima, T.; Isoya, J.; Wrachtrup, J. Subpicotesla diamond magnetometry. *Phys. Rev. X* **2015**, *5*, 041001.
- (19) Barry, J. F.; Schloss, J. M.; Bauch, E.; Turner, M. J.; Hart, C. A.; Pham, L. M.; Walsworth, R. L. Sensitivity optimization for nv-diamond magnetometry. *Rev. Mod. Phys.* **2020**, *92*, 015004.
- (20) Scholten, S. C.; Healey, A. J.; Robertson, I. O.; Abrahams, G. J.; Broadway, D. A.; Tetteen, J.-P. Widefield quantum microscopy with nitrogen-vacancy centers in diamond: Strengths, limitations, and prospects. *J. Appl. Phys.* **2021**, *130*, 150902.
- (21) Devienne, S. J.; Pham, L. M.; Lovchinsky, I.; Sushkov, A. O.; Bar-Gill, N.; Belthangady, C.; Casola, F.; Corbett, M.; Zhang, H.; Lukin, M.; Park, H.; Yacoby, A.; Walsworth, R. L. Nanoscale NMR spectroscopy and imaging of multiple nuclear species. *Nat. Nanotechnol.* **2015**, *10*, 129.
- (22) Thiel, L.; Wang, Z.; Tschudin, M. A.; Rohner, D.; Gutiérrez-Lezama, I.; Ubrig, N.; Gibertini, M.; Giannini, E.; Morpurgo, A. F.; Maletinsky, P. Probing magnetism in 2D materials at the nanoscale with single-spin microscopy. *Science* **2019**, *364*, 973.
- (23) Rovny, J.; Yuan, Z.; Fitzpatrick, M.; Abdalla, A. I.; Futamura, L.; Fox, C.; Cambria, M. C.; Kolkowitz, S.; de Leon, N. P. Nanoscale covariance magnetometry with diamond quantum sensors. *Science* **2022**, *378*, 1301.
- (24) Riedel, D.; Söllner, I.; Shields, B. J.; Starosielec, S.; Appel, P.; Neu, E.; Maletinsky, P.; Warburton, R. J. Deterministic enhancement of coherent photon generation from a nitrogen-vacancy center in ultrapure diamond. *Phys. Rev. X* **2017**, *7*, 031040.
- (25) Körber, J.; Pallmann, M.; Heupel, J.; Stöhr, R.; Vasilenko, E.; Hümmer, T.; Kohler, L.; Popov, C.; Hunger, D. Scanning Cavity Microscopy of a Single-Crystal Diamond Membrane. *Phys. Rev. Appl.* **2023**, *19*, 064057.
- (26) Herrmann, Y.; Fischer, J.; Brevoord, J. M.; Sauerzapf, C.; Wienhoven, L. G. C.; Feije, L. J.; Pasini, M.; Eschen, M.; Ruf, M.; Weaver, M. J.; Hanson, R. Coherent Coupling of a Diamond Tin-Vacancy Center to a Tunable Open Microcavity. *Phys. Rev. X* **2024**, *14*, 41013.
- (27) Yurgens, V.; Fontana, Y.; Corazza, A.; Shields, B. J.; Maletinsky, P.; Warburton, R. J. Cavity-assisted resonance fluorescence from a nitrogen-vacancy center in diamond. *npj Quantum Inf* **2024**, *10*, 112.
- (28) Berghaus, R.; Sachero, S.; Bayer, G.; Heupel, J.; Herzig, T.; Feuchtmayr, F.; Meijer, J.; Popov, C.; Kubanek, A. Cavity-enhanced emission and absorption of color centers in a diamond membrane with selectable strain. *Phys. Rev. Appl.* **2025**, *23*, 034050.
- (29) Maletinsky, P.; Hong, S.; Grinolds, M. S.; Hausmann, B.; Lukin, M. D.; Walsworth, R. L.; Loncar, M.; Yacoby, A. A robust scanning diamond sensor for nanoscale imaging with single nitrogen-vacancy centres. *Nat. Nanotechnol.* **2012**, *7*, 320.
- (30) Appel, P.; Neu, E.; Ganzhorn, M.; Barfuss, A.; Batzer, M.; Gratz, M.; Tschöpe, A.; Maletinsky, P. Fabrication of all diamond scanning probes for nanoscale magnetometry. *Rev. Sci. Instrum.* **2016**, *87*, 063703.
- (31) Zhou, T. X.; Stöhr, R. J.; Yacoby, A. Scanning diamond NV center probes compatible with conventional AFM technology. *Appl. Phys. Lett.* **2017**, *111*, 163106.
- (32) Hedrich, N.; Rohner, D.; Batzer, M.; Maletinsky, P.; Shields, B. J. Parabolic diamond scanning probes for single-spin magnetic field imaging. *Phys. Rev. Appl.* **2020**, *14*, 064007.
- (33) Khanaliloo, B.; Jayakumar, H.; Hryciw, A. C.; Lake, D. P.; Kaviani, H.; Barclay, P. E. Single-crystal diamond nanobeam waveguide optomechanics. *Phys. Rev. X* **2015**, *5*, 041051.
- (34) Ali Momenzadeh, S.; De Oliveira, F. F.; Neumann, P.; Bhaktavatsala Rao, D. D.; Denisenko, A.; Amjadi, M.; Chu, Z.; Yang, S.; Manson, N. B.; Doherty, M. W.; Wrachtrup, J. Thin Circular Diamond Membrane with Embedded Nitrogen-Vacancy Centers for Hybrid Spin-Mechanical Quantum Systems. *Phys. Rev. Appl.* **2016**, *6*, 024026.
- (35) Héritier, M.; Eichler, A.; Pan, Y.; Grob, U.; Shorubalko, I.; Krass, M. D.; Tao, Y.; Degen, C. L. Nanoladder cantilevers made from diamond and silicon. *Nano Lett.* **2018**, *18*, 1814.
- (36) Li, X.; Lekavicius, I.; Noeckel, J.; Wang, H. Ultracoherent gigahertz diamond spin-mechanical lamb wave resonators. *Nano Lett.* **2024**, *24*, 10995.
- (37) Joe, G.; Chia, C.; Pingault, B.; Haas, M.; Chalupnik, M.; Cornell, E.; Kuruma, K.; Machielse, B.; Sinclair, N.; Meesala, S.; Lončar, M. High q-factor diamond optomechanical resonators with silicon vacancy centers at millikelvin temperatures. *Nano Lett.* **2024**, *24*, 6831.
- (38) Evans, R. E.; Bhaskar, M. K.; Sukachev, D. D.; Nguyen, C. T.; Sipahigil, A.; Burek, M. J.; Machielse, B.; Zhang, G. H.; Zibrov, A. S.; Bielejec, E.; Park, H.; Lončar, M.; Lukin, M. D. Photon-mediated interactions between quantum emitters in a diamond nanocavity. *Science* **2018**, *362*, 662.
- (39) Machielse, B.; Bogdanovic, S.; Meesala, S.; Gauthier, S.; Burek, M. J.; Joe, G.; Chalupnik, M.; Sohn, Y. I.; Holzgrafe, J.; Evans, R. E.; Chia, C.; Atikian, H.; Bhaskar, M. K.; Sukachev, D. D.; Shao, L.; Maity, S.; Lukin, M. D.; Lončar, M. Quantum interference of electromechanically stabilized emitters in nanophotonic devices. *Phys. Rev. X* **2019**, *9*, 031022.
- (40) Knaut, C. M.; Suleymanzade, A.; Wei, Y. C.; Assumpcao, D. R.; Stas, P. J.; Huan, Y. Q.; Machielse, B.; Knall, E. N.; Sutula, M.; Baranes, G.; Sinclair, N.; De-Eknamkul, C.; Levonian, D. S.; Bhaskar, M. K.; Park, H.; Lončar, M.; Lukin, M. D. Entanglement of nanophotonic quantum memory nodes in a telecom network. *Nature* **2024**, *629*, 573.
- (41) Ding, S. W.; Haas, M.; Guo, X.; Kuruma, K.; Jin, C.; Li, Z.; Awschalom, D. D.; Deegan, N.; Heremans, F. J.; High, A. A.; Loncar, M. High-Q cavity interface for color centers in thin film diamond. *Nat. Commun.* **2024**, *15*, 6358.

- (42) Sangtawesin, S.; Dwyer, B. L.; Srinivasan, S.; Allred, J. J.; Rodgers, L. V.; De Greve, K.; Stacey, A.; Dontschuk, N.; O'Donnell, K. M.; Hu, D.; Evans, D. A.; Jaye, C.; Fischer, D. A.; Markham, M. L.; Twitchen, D. J.; Park, H.; Lukin, M. D.; De Leon, N. P. Origins of Diamond Surface Noise Probed by Correlating Single-Spin Measurements with Surface Spectroscopy. *Phys. Rev. X* **2019**, *9*, 031052.
- (43) Yu, X.; Villafranca, E. J.; Wang, S.; Jones, J. C.; Xie, M.; Nagura, J.; Chi-Durán, I.; Deegan, N.; Martinson, A. B. F.; Flatté, M. E.; Candido, D. R.; Galli, G.; Maurer, P. C. Engineering dark spin-free diamond interfaces. *arXiv Preprint*, arXiv:2504.08883, 3 May 2025.
- (44) Toros, A.; Kiss, M.; Graziosi, T.; Mi, S.; Berrazouane, R.; Naamoun, M.; Vukajlovic Plestina, J.; Gallo, P.; Quack, N. Reactive ion etching of single crystal diamond by inductively coupled plasma: State of the art and catalog of recipes. *Diam. Relat. Mater.* **2020**, *108*, 107839.
- (45) Mi, S.; Kiss, M.; Graziosi, T.; Quack, N. Integrated photonic devices in single crystal diamond. *J. Phys. Photonics* **2020**, *2*, 042001.
- (46) Rani, D.; Opaluch, O. R.; Neu, E. Recent advances in single crystal diamond device fabrication for photonics, sensing and nanomechanics. *Micromachines* **2021**, *12*, 36.
- (47) Burek, M. J.; Chu, Y.; Liddy, M. S.; Patel, P.; Rochman, J.; Meesala, S.; Hong, W.; Quan, Q.; Lukin, M. D.; Lončar, M. High quality-factor optical nanocavities in bulk single-crystal diamond. *Nat. Commun.* **2014**, *5*, 5718.
- (48) Latawiec, P.; Burek, M. J.; Sohn, Y.-I.; Lončar, M. Faraday cage angled-etching of nanostructures in bulk dielectrics. *J. Vac. Sci. Technol. B* **2016**, *34*, 041801.
- (49) Atikian, H. A.; Latawiec, P.; Burek, M. J.; Sohn, Y.-I.; Meesala, S.; Gravel, N.; Kouki, A. B.; Lončar, M. Freestanding nanostructures via reactive ion beam angled etching. *APL Photonics* **2017**, *2*, 051301.
- (50) Khanaliloo, B.; Mitchell, M.; Hryciw, A. C.; Barclay, P. E. High-Q/V Monolithic Diamond Microdisks Fabricated with Quasi-isotropic Etching. *Nano Lett.* **2015**, *15*, 5131.
- (51) Mouradian, S.; Wan, N. H.; Schröder, T.; Englund, D. Rectangular photonic crystal nanobeam cavities in bulk diamond. *Appl. Phys. Lett.* **2017**, *111*, 021103.
- (52) Kuruma, K.; Pingault, B.; Chia, C.; Haas, M.; Joe, G. D.; Assumpcao, D. R.; Ding, S. W.; Jin, C.; Xin, C. J.; Yeh, M.; Sinclair, N.; Lončar, M. Controlling interactions between high-frequency phonons and single quantum systems using phononic crystals. *Nat. Phys.* **2025**, *21*, 77–82.
- (53) Magyar, A. P.; Lee, J. C.; Limarga, A. M.; Aharonovich, I.; Rol, F.; Clarke, D. R.; Huang, M.; Hu, E. L. Fabrication of thin, luminescent, single-crystal diamond membranes. *Appl. Phys. Lett.* **2011**, *99*, 081913.
- (54) Aharonovich, I.; Lee, J. C.; Magyar, A. P.; Buckley, B. B.; Yale, C. G.; Awschalom, D. D.; Hu, E. L. Homoepitaxial growth of single crystal diamond membranes for quantum information processing. *Adv. Mater.* **2012**, *24*, OP54.
- (55) Guo, X.; Deegan, N.; Karsch, J. C.; Li, Z.; Liu, T.; Shreiner, R.; Butcher, A.; Awschalom, D. D.; Heremans, F. J.; High, A. A. Tunable and Transferable Diamond Membranes for Integrated Quantum Technologies. *Nano Lett.* **2021**, *21*, 10392.
- (56) Scheuner, C.; Kuhrke, M.; Lühmann, T.; Kieschnick, M.; Reiß, S.; Engel, J.; Bähr, M.; Pezzagna, S.; Meijer, J. Creation of diamond membranes containing nitrogen-vacancy centers by means of ion irradiation. *J. Appl. Phys.* **2024**, *136*, 044402.
- (57) Guo, X.; Xie, M.; Addhya, A.; Linder, A.; Zvi, U.; Wang, S.; Yu, X.; Deshmukh, T. D.; Liu, Y.; Hammock, I. N.; Li, Z.; DeVault, C. T.; Butcher, A.; Esser-Kahn, A. P.; Awschalom, D. D.; Deegan, N.; Maurer, P. C.; Heremans, F. J.; High, A. A. Direct-bonded diamond membranes for heterogeneous quantum and electronic technologies. *Nat. Commun.* **2024**, *15*, 8788.
- (58) Heupel, J.; Pallmann, M.; Körber, J.; Hunger, D.; Reithmaier, J. P.; Popov, C. Fabrication of high-quality thin single-crystal diamond membranes with low surface roughness. *Phys. Status Solidi A* **2023**, *220*, 2200465.
- (59) Hoekstra, R. J.; Kushner, M. J.; Sukharev, V.; Schoenborn, P. Microtrenching resulting from specular reflection during chlorine etching of silicon. *J. Vac. Sci. Technol. B* **1998**, *16*, 2102.
- (60) Challier, M.; Sonusen, S.; Barfuss, A.; Rohner, D.; Riedel, D.; Koelbl, J.; Ganzhorn, M.; Appel, P.; Maletinsky, P.; Neu, E. Advanced fabrication of single-crystal diamond membranes for quantum technologies. *Micromachines* **2018**, *9*, 148.
- (61) Riedrich-Möller, J.; Kipfstuhl, L.; Hepp, C.; Neu, E.; Pauly, C.; Mücklich, F.; Baur, A.; Wandt, M.; Wolff, S.; Fischer, M.; Gsell, S.; Schreck, M.; Becher, C. One- and two-dimensional photonic crystal microcavities in single crystal diamond. *Nat. Nanotechnol.* **2012**, *7*, 69.
- (62) Jung, T.; Görlitz, J.; Kambs, B.; Pauly, C.; Raatz, N.; Nelz, R.; Neu, E.; Edmonds, A. M.; Markham, M.; Mücklich, F.; Meijer, J.; Becher, C. Spin measurements of NV centers coupled to a photonic crystal cavity. *APL Photonics* **2019**, *4*, 120803.
- (63) Yamada, T.; Yoshikawa, H.; Uetsuka, H.; Kumaragurubaran, S.; Tokuda, N.; Shikata, S.-i. Cycle of two-step etching process using ICP for diamond MEMS applications. *Diam. Relat. Mater.* **2007**, *16*, 996.
- (64) Toros, A.; Kiss, M.; Graziosi, T.; Sattari, H.; Gallo, P.; Quack, N. Precision micro-mechanical components in single crystal diamond by deep reactive ion etching. *Microsyst. Nanoeng.* **2018**, *4*, 12.
- (65) Heupel, J.; Pallmann, M.; Körber, J.; Merz, R.; Kopnarski, M.; Stöhr, R.; Reithmaier, J. P.; Hunger, D.; Popov, C. Fabrication and characterization of single-crystal diamond membranes for quantum photonics with tunable microcavities. *Micromachines* **2020**, *11*, 1080.
- (66) Fuchs, P.; Jung, T.; Kieschnick, M.; Meijer, J.; Becher, C. A cavity-based optical antenna for color centers in diamond. *APL Photonics* **2021**, *6*, 086102.
- (67) Flågan, S.; Riedel, D.; Javadi, A.; Jakubczyk, T.; Maletinsky, P.; Warburton, R. J. A diamond-confined open microcavity featuring a high quality-factor and a small mode-volume. *J. Appl. Phys.* **2022**, *131*, 113102.
- (68) Barclay, P. E.; Fu, K.-M.; Santori, C.; Beausoleil, R. G. Hybrid photonic crystal cavity and waveguide for coupling to diamond NV-centers. *Opt. Express* **2009**, *17*, 9588.
- (69) Huang, D.; Abulnaga, A.; Welinski, S.; Raha, M.; Thompson, J. D.; de Leon, N. P. Hybrid III-V diamond photonic platform for quantum nodes based on neutral silicon vacancy centers in diamond. *Opt. Express* **2021**, *29*, 9174.
- (70) Chakravarthi, S.; Yama, N. S.; Abulnaga, A.; Huang, D.; Pederson, C.; Hestroffer, K.; Hatami, F.; de Leon, N. P.; Fu, K.-M. C. Hybrid integration of gap photonic crystal cavities with silicon-vacancy centers in diamond by stamp-transfer. *Nano Lett.* **2023**, *23*, 3708.
- (71) Palm, K. J.; Dong, M.; Golter, D. A.; Clark, G.; Zimmermann, M.; Chen, K. C.; Li, L.; Menssen, A.; Leenheer, A. J.; Dominguez, D.; et al. Modular chip-integrated photonic control of artificial atoms in diamond waveguides. *Optica* **2023**, *10*, 634.
- (72) Kasperczyk, M.; Zuber, J. A.; Barfuss, A.; Kölbl, J.; Yurgens, V.; Flågan, S.; Jakubczyk, T.; Shields, B.; Warburton, R. J.; Maletinsky, P. Statistically modeling optical linewidths of nitrogen vacancy centers in microstructures. *Phys. Rev. B* **2020**, *102*, 75312.
- (73) Yurgens, V.; Corazza, A.; Zuber, J. A.; Gruet, M.; Kasperczyk, M.; Shields, B. J.; Warburton, R. J.; Fontana, Y.; Maletinsky, P. Spectrally stable nitrogen-vacancy centers in diamond formed by carbon implantation into thin microstructures. *Appl. Phys. Lett.* **2022**, *121*, 234001.
- (74) Ruf, M.; IJspeert, M.; Van Dam, S.; De Jong, N.; Van Den Berg, H.; Evers, G.; Hanson, R. Optically coherent nitrogen-vacancy centers in micrometer-thin etched diamond membranes. *Nano Lett.* **2019**, *19*, 3987.